Journal of Controlled Release 393 (2026) 114750

Contents lists available at ScienceDirect

Journal of Controlled Release

journal homepage: www.elsevier.com/locate/jconrel

# Low-dose radiation generated ROS-activatable doxorubicin prodrug loaded liposome nanoparticles for triple-negative breast cancer treatment☆

Hwanju Lim [a,b,1], Yujeong Moon [b,1], Sangheon Han [c,1], Hanhee Cho [b,d,1], Sunejeong Song [b], Jinseong Kim [b], Jagyeong Goo [a], Nayeon Shim [b], Lili Guo [e], Tae-il Kim [e], Won Seok Chang [c,*], Won-Gun Koh [a,*], Kwangmeyung Kim [b,f,*]

[a] Department of Chemical and Biomolecular Engineering, Yonsei University, Seoul 03722, Republic of Korea
[b] College of Pharmacy, Graduate School of Pharmaceutical Sciences, Ewha Womans University, Seoul 03760, Republic of Korea
[c] Department of Neurosurgery, College of Medicine, Yonsei University, Seoul 03722, Republic of Korea
[d] Noxpharm Co., LTD., Seoul 03759, Republic of Korea
[e] School of Chemical Engineering, Sungkyunkwan University, Suwon 16419, Republic of Korea
[f] Graduate Program in Innovative Biomaterials Convergence, Ewha Womans University, Seoul 03760, Republic of Korea

ARTICLE INFO

*Keywords:*
Triple-negative breast cancer
Stimuli-responsive nanomedicine
Activable doxorubicin prodrug
Chemoradiotherapy
Reactive oxygen species
Immunogenic cell death

ABSTRACT

Triple-negative breast cancer (TNBC) treatment is frequently limited by both intrinsic resistance and normal tissue toxicity in radiation therapy (RT) and chemotherapy. Herein, we report reactive oxygen species (ROS)-activatable DOX prodrug loaded liposome nanoparticles (ROS-LNPs) for precision therapy against TNBC. First, the ROS-activatable DOX prodrug was prepared by chemically conjugating caspase-3-cleavable peptide (Acetyl-*Lys-Gly-Asp-Glu-Val-Asp*, KGDEVD) to DOX using self-immolative PABC linker, resulting in DEVD-DOX. The prodrug of DEVD-DOX is inactive and nontoxic in cancer cells, but it exhibits ROS-activatable cytotoxicity following low-dose radiation. Second, DEVD-DOX is encapsulated into 1,2-dioleoyl-sn-glycero-3-phospho-L-serine (PS)-containing liposome nanoparticles (ROS-LNPs) to improve blood stability and uniformly penetrate into tumor tissue. The resulting ROS-LNPs form very stable nanoparticles with an average diameter of 108.1 ± 7.3 nm. In particular, ROS-LNPs exhibit low-dose radiation (5 Gy) generated ROS-activatable cytotoxicity in 4 T1 cells, wherein ROS-induced activated caspase-3 can cleave DEVD-DOX released from ROS-LNPs into free DOX that further shows the ROS-induced amplified cytotoxicity without lose-dose radiation. To overcome physiological barriers of the tumor targeting of ROS-LNPs in tumor microenvironment (TME), micro-syringe chip (MSC)-mediated intratumoral delivery strategy is employed to ensure uniform intratumoral delivery. MSC-mediated intratumoral administration of ROS-LNPs exhibit 3.26-fold higher tumor-targeting efficiency than conventional intratumoral administration in 4 T1 tumor-bearing mice. The combination of ROS-LNPs and low-dose radiation greatly suppresses tumor growth with potential anticancer immunity, such elevated ICD, dendritic cell (DC) activation, and cytotoxic T cell infiltration, in 4 T1 tumor-bearing mice. Furthermore, the combination of ROS-LNPs and low-dose radiation exhibits the minimal off-target toxicity in normal tissues. This study highlights the clinical potential of ROS-activable doxorubicin loaded liposome nanoparticles as a promising stimulus-responsive platform to bridge the gap between low-dose RT and precision chemotherapy in TNBC treatment.

## 1. Introduction

Triple-negative breast cancer (TNBC) represents the most aggressive subtype, accounting for approximately 15% of all cases and associated with poor prognosis, early recurrence, and high metastatic potential [1–4]. The absence of estrogen receptor (ER), progesterone receptor (PR), and human epidermal growth factor receptor 2 (HER2), TNBC has significant limitations on the application of conventional targeted

☆ This article is part of a Special issue entitled: 'Reactive oxygen species for advanced drug delivery' published in Journal of Controlled Release.

* Corresponding authors.
*E-mail addresses:* changws0716@yuhs.ac (W.S. Chang), wongun@yonsei.ac.kr (W.-G. Koh), kimkm@ewha.ac.kr (K. Kim).

[1] These authors contributed equally to this work.

https://doi.org/10.1016/j.jconrel.2026.114750
Received 30 December 2025; Received in revised form 7 February 2026; Accepted 23 February 2026
Available online 27 February 2026

therapies in TNBC [5–7]. Consequently, chemotherapy remains the primary treatment option, but the efficacy of chemotherapeutic agents such as doxorubicin (DOX) is usually restricted by low tumor targeting efficacy and severe toxicity to normal tissues [8,9]. Notably, the clinical trials of DOX is limited by cardiotoxicity and splenic toxicity, as both toxicities trigger systemic immunosuppression [10–12]. In addition, the immunosuppressive tumor microenvironment (TME) of TNBC enriched with cancer-associated fibroblasts, myeloid-derived suppressor cells, and tumor-associated M2 macrophages form physical barrier that inhibits antitumor immunity and restricts drug penetration into the tumor core [13,14]. This limited drug accumulation in TNBC often fails to trigger robust apoptotic pathways, ultimately contributing to the development of chemoresistance [15].

To address these challenges, liposomal delivery systems have been developed to enhance the targeted delivery of DOX while decreasing its off-target toxicity [16,17]. Clinical evaluations have confirmed that DOX loaded liposome nanoparticles (LNPs) could effectively suppress solid tumor growth with a manageable safety profile [18]. Nevertheless, several limitations still exist, such as inadequate tumor selectivity and prolonged toxicity in healthy organs, which often result in modest therapeutic outcomes [19]. Specifically, non-specific interactions with blood components and rapid clearance by the reticuloendothelial system

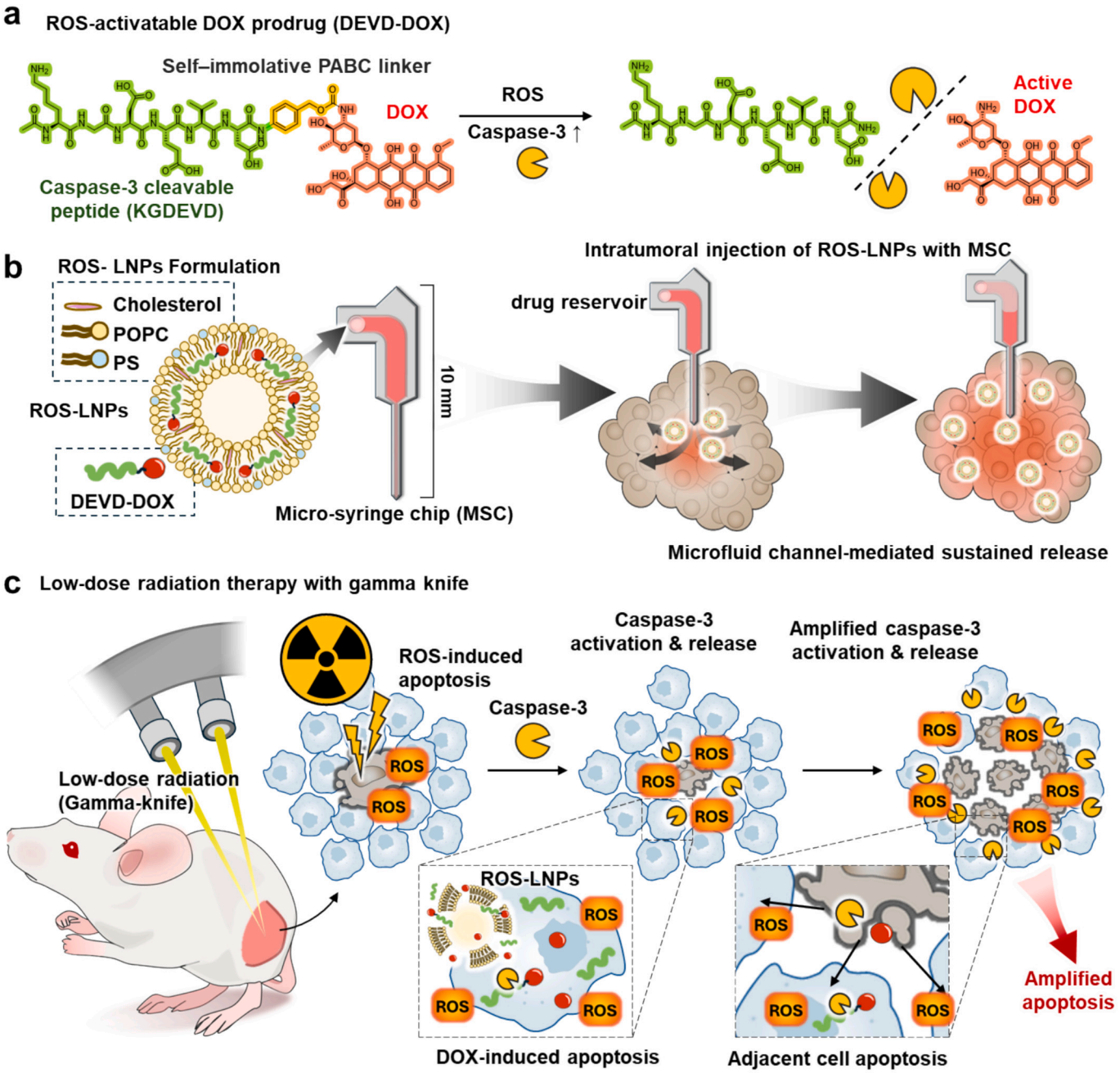


**Scheme 1. Schematic illustration of the design and low-radiation generated ROS-activatable apoptosis mechanism of ROS-LNPs for enhanced TNBC treatment.** (a) DEVD-DOX are prepared through the chemical conjugation of a caspase-3-cleavable KGDEVD peptide to DOX *via* a self-immolative PABC linker. (b) ROS-LNPs are formulated by encapsulating the prodrug into PS-containing LNPs and are intratumorally administered using MSC to ensure uniform intratumoral distribution and maximize local drug accumulation while minimizing systemic exposure. (c) Upon focused low-dose radiation, generated ROS initiate initial cancer cell apoptosis and activate caspase-3, which triggers the rapid release of active DOX to establish a self-amplifying cell death cycle that effectively overcomes persistent radioresistance and systemic toxicity of RT and chemotherapy in the treatment of aggressive TNBC.

(RES) severely impede the passive targeting ability of DOX loaded LNPs in many preclinical models [20]. Accordingly, recent reports have shown that only approximately 1–2% of administered DOX loaded LNPs actually reach the targeted tumor tissue [21]. Even for small amount of DOX loaded LNPs that reaches the tumor, physiological barriers, such as high interstitial fluid pressure and complex extracellular matrix (ECM) further restricted the deep penetration of LNPs into the tumor tissues [22]. Crucially, conventional drug-loaded LNPs lack a precise drug release mechanism, leading to premature DOX leakage and persistent systemic toxicity [23]. These problems of liposomal delivery systems highlight the urgent need for novel delivery platforms that integrate robust tumor targeting and site-specific activation of anticancer drug to eliminate off-target toxicity.

Radiation therapy (RT) is used as neoadjuvant therapy before surgery or as adjuvant therapy after surface for TNBC to reduce tumor size and recurrence risk. In general, high-dose RT with 10 Gy primarily kills cancer cells by generating reactive oxygen species (ROS) that induce oxidative stress and DNA damage [24]. However, tumors often develop radioresistance through antioxidant systems like the Nrf2 pathway, which neutralizes ROS to maintain redox homeostasis, promoting expression of protective enzymes such as heme oxygenase 1 [25]. Consequently, the efficacy of high-dose RT is constrained by both intrinsic resistance and collateral toxicity to normal tissues, such as fibrosis and cardiopulmonary injury [26]. In the case of TNBC, this resistance often stems from efficient DNA repair and immunosuppressive TME enriched with regulatory T cells [27]. To mitigate these risks, studies have been conducted on the ability of low-dose radiation to modulate the TEM and stimulate anti-tumor immunity through immunogenic cell death (ICD) [28]. Although this low-dose radiation-induced ICD promotes the release of damage-associated molecular patterns (DAMPs) to enhance immune cell infiltration, low-dose radiation alone is generally insufficient to effectively eradicate aggressive TNBC. These conflicting factors highlight the need for innovative strategies that can leverage the immune-activating effects of low-dose radiation while simultaneously amplifying its insufficient cancer cell killing capacity in the treatment of TNBC.

Herein, we developed low-dose radiation generated ROS-activatable DOX prodrug loaded liposome nanoparticles (ROS-LNPs) for cancer cell-specific and sufficient apoptosis even with low-dose radiation (5Gy) for TNBC treatment. First, the ROS-activatable DOX prodrug was prepared by chemically conjugating caspase-3-cleavable peptide (Acetyl-*Lys-Gly-Asp-Glu-Val-Asp*, KGDEVD) to DOX using self-immolative PABC linker, resulting in DEVD-DOX (Scheme 1a). The prodrug of DEVD-DOX is inactive and nontoxic in cancer cells, but it exhibits ROS-activatable cytotoxicity following ROS generation *via* low-dose radiation. This is because DEVD peptide in the prodrug is specifically cleaved by ROS-induced active caspase-3 that is a crucial executioner enzyme in apoptosis and then free DOX, whose peptide is cleaved, further activates DEVD-DOX, thereby inducing ROS-induced amplified apoptosis mechanism of DEVD-DOX after low-dose radiation [29–35]. Next, DEVD-DOX was encapsulated into 1,2-dioleoyl-sn-glycero-3-phospho-L-serine (PS)-containing liposome nanoparticles (ROS-LNPs) to improve blood stability and uniformly penetrate into tumor tissue. Second, to increase targeting efficiency, we intratumorally inject ROS-LNPs using microsyringe chip (MSC) with drug reservoir and microfluid channel (Scheme 1b). Importantly, ROS-LNPs loaded in drug reservoir of MSC are very slowly injected into targeted tumor tissues through microchannel for long-time period. We already confirmed that MSC-guided intratumoral administration of PS-containing LNPs greatly increased the tumor targeting efficiency with a uniform intratumoral distribution, compared to conventional intravenous or intratumoral administration, thereby maximizing local accumulation of LNPs in tumor tissues [36]. Subsequently, low-dose focused radiation (5 Gy) through a gamma knife is applied to the tumor tissues, leading to ROS-activatable cancer cell death of ROS-LNPs while protecting normal tissues from serious toxicity (Scheme 1c). Importantly, focused low-dose radiation elevates intratumoral caspase-3 levels, which in turn cleaves the DEVD peptide in the prodrug released from ROS-LNPs, thereby activating the cytotoxicity of free DOX only in the targeted tumor tissues. Finally, the ROS-activated free DOX also produces large amount of ROS that further activates DEVD-DOX, and induces ROS-induced amplified apoptosis mechanism of ROS-LNPs in targeted tumor tissues.

By combining low-dose generated ROS-activatable ROS-LNPs with focused low-dose radiation, our approach aims to overcome the radioresistance of current high-dose RT in TNBC treatment and to achieve robust anti-tumor efficacy without incurring systemic toxicity. Therefore, the ROS-induced amplified apoptosis mechanism of ROS-LNPs with low-dose radiation can overcome the serious challenges associated with radioresistance and systemic toxicity of high-dose radiation for TNBC treatment. In this study, the nanoparticle structure and the caspase-3-specific activation mechanism of ROS-LNPs were characterized in cell culture system. Their ability to induce effective ROS-induced amplified apoptosis mechanism was validated in 4 T1 TNBC cells, in which low-dose radiation triggered the release of free DOX *via* the ROS-induced caspase-3 pathway. In this study, 4 T1 was chosen as an immune-cold TNBC model in immunocompetent syngeneic hosts to enable evaluation of ICD-linked immune effects [37,38]. The therapeutic efficacy and safety of ROS-LNPs were evaluated in 4 T1 tumor xenograft models through a combination of MSC-mediated intratumoral delivery and focused low-dose radiation, simultaneously.

## 2. Results and discussion

### 2.1. Preparation and characterization of ROS-activatable prodrug-loaded liposome nanoparticles (ROS-LNPs)

Current RT with high-dose radiation can induce severe cancer cell death by generating sufficient ROS that induces severe oxidative stress and DNA damage. However, high-dose radiation in TNBC treatment usually causes radioresistance and collateral toxicity to normal tissues. To migrate these risks, we developed low-dose radiation generated ROS-activatable DOX prodrug loaded liposome nanoparticles (ROS-LNPs) that can exhibit cancer cell-specific and sufficient apoptosis even with low-dose radiation. Firstly, the ROS-activatable DOX prodrug is synthesized by chemically conjugating caspase-3-cleavable peptide (Acetyl-*Lys-Gly-Asp-Glu-Val-Asp*, KGDEVD) to DOX with a self-immolative linker (PABC). We have already reported that various prodrugs containing caspase-3 cleavable DEVD peptide showed the caspase-3-activatable cytotoxicity in photodynamic therapy (PDT) and RT [39,40]. In principle, DEVD-conjugated DOX or DEVD-conjugated monomethyl auristatin E (MMAE) is not toxic as inactive form in live cancer cells. However, each prodrug is cleaved by active caspase produced by visible light or radiation and the cleaved free DOX or MMAE shows highly potent apoptosis, thereby inducing the caspase-3-activatable apoptosis mechanism of prodrugs. In detail, the protected KGDEVD peptide was first coupled to a p-aminobenzyl alcohol (PABA) moiety and subsequently activated into a reactive carbonate intermediate (pKGDEVD-PABC) (**Fig. S1**). And, DOX was then conjugated to this activated pKGDEVD-PABC linker with high coupling efficiency, followed by the palladium-catalyzed removal of the alloc and allyl protecting groups to afford the final DEVD-DOX. The crude product was purified *via* preparative HPLC and subsequently lyophilized to afford the final DEVD-DOX as a red powder (136 mg, 12.2% yield). Analytical HPLC confirmed a purity of 98.7%, while LC-MS verified the expected molecular weight of 1377.8 $[M + H]^+$ (**Fig. S2**).

Next, for the preparation of ROS-activatable prodrug-loaded liposome nanoparticles (ROS-LNPs), 1-palmitoyl-2-oleoyl-sn-glycero-3-phosphocholine (POPC), cholesterol, negatively charged PS and DEVD-DOX were dissolved in ethanol at a molar ratio of 72.2:5.64:10.86:11.28, followed by film hydration with PBS at 40 °C for 30 min (Fig. 1a). The prepared ROS-LNPs exhibited a uniform liposome architecture with a mean hydrodynamic diameter of 108.1 ± 7.3 nm (*n*

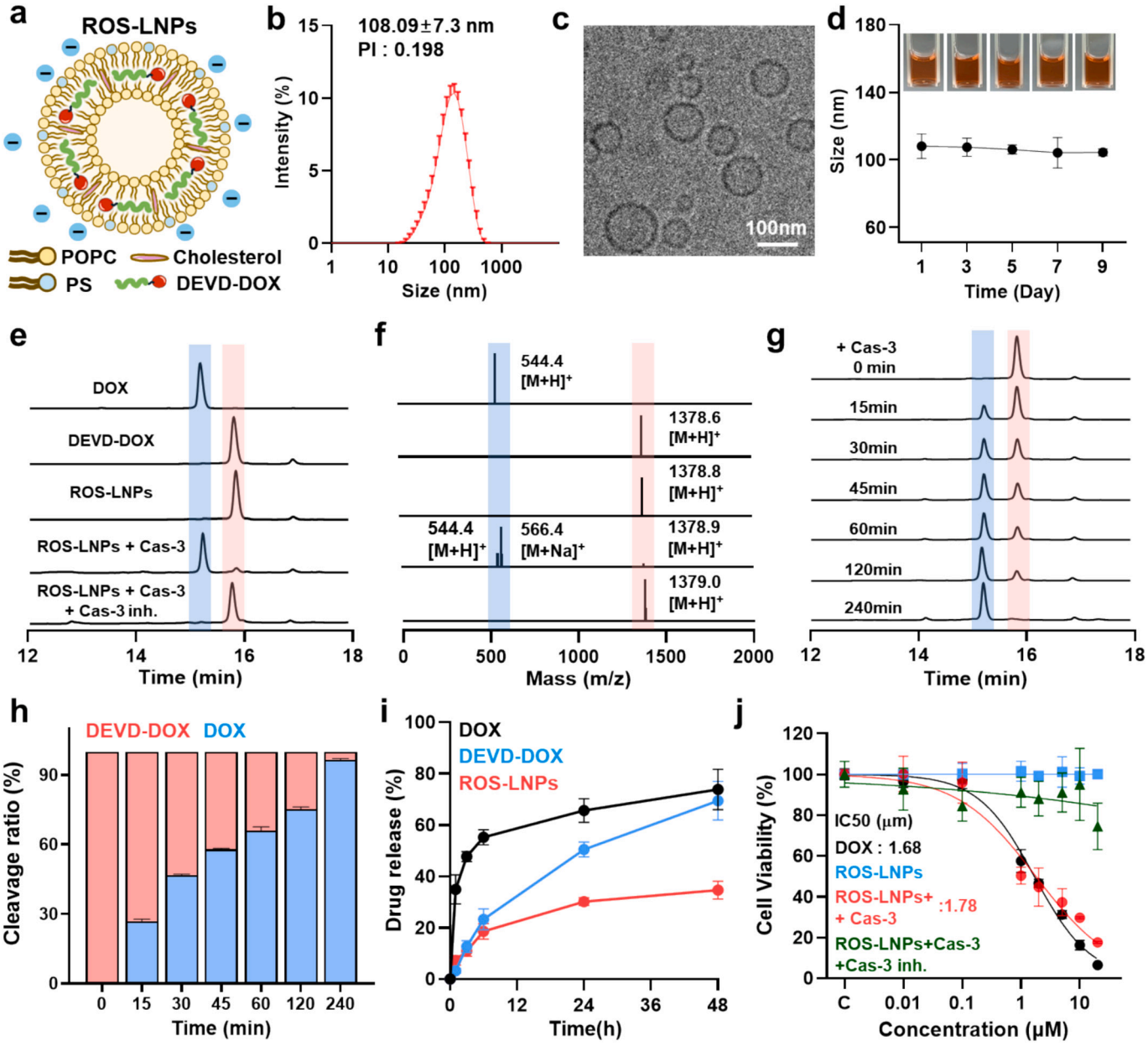


**Fig. 1. Physicochemical characterization and caspase-3-specific drug activation of ROS-LNPs.** (a) Schematic illustration of DEVD-DOX-containing PS liposomes (ROS-LNPs) with negative surface charge. (b) Hydrodynamic size distribution of ROS-LNPs in saline (1 mg/mL, based on DOX) measured by DLS. (c) TEM image showing the structural morphology of ROS-LNPs in DW (1 mg/mL, based on DOX). (d) Colloidal stability of ROS-LNPs in saline at 37 °C monitored for 9 days. (e) HPLC analysis of ROS-LNPs following incubation with recombinant caspase-3 (12.5 μg/mL). (f) Mass spectrum confirming the release of active DOX after enzymatic cleavage. (g) Time-dependent HPLC profiles showing the conversion of ROS-LNPs to free DOX. (h) Quantitative analysis of the time-dependent conversion of ROS-LNPs to free DOX from. (i) Comparative drug release kinetics of free DOX, DEVD-DOX, and ROS-LNPs using a dialysis membrane (MWCO: 12 kDa). (j) Caspase-3-dependent cytotoxicity of various formulations in 4 T1 TNBC cells. In (d, h, i, j), data are presented as the mean ± SD ($n = 3$).

$= 3$) determined with DLS measurement (Fig. 1b). The Cryo-TEM image further confirmed the spherical morphology and homogeneous size distribution of ROS-LNPs (Fig. 1c**).** The encapsulation efficiency of DEVD-DOX in ROS-LNPs was 90.1 ± 3.4% **(Fig. S3)**. The surface charge was −29.32 ± 0.12 mV, which was attributed to the negatively charged head group of PS and negatively charged DEVD peptide **(Fig. S4)**. Importantly, ROS-LNPs displayed high colloidal stability in saline with negligible changes in nanoparticle size over 9 days, indicating robust physiological stability (Fig. 1d). This enhanced stability is expected to facilitate efficient retention and accumulation of ROS-LNPs within tumor tissues under *in vivo* conditions [41–43]. The caspapse-3-specific cleavage of DEVD-DOX (1 mg/mL) and ROS-LNPs (1 mg/ml) was tested in the presence of active caspase-3 (12.5 μg/mL). Characteristic HPLC peaks of DEVD-DOX and ROS-LNPs appeared at 1378.8 $[M + H]^+$, suggesting that the acetonitrile-$H_2O$ mobile phase of HPLC disrupted the liposomal structure. Upon incubation of ROS-LNPs with recombinant caspase-3 in PBS, a distinct new peak corresponding to free DOX (544.4 $[M + H]^+$ and 566.4 $[M + Na]^+$) emerged at 15.2 min after 4 h, confirming successful enzymatic cleavage (Fig. 1e and f). In contrast, when ROS-LNPs (1 mg/ml) were pre-treated with an irreversible caspase-3 inhibitor (12.5 μg/mL), no cleavage was observed despite the presence of caspase-3. Time-dependent HPLC analysis further demonstrated that free DOX release initiated within 15 min of co-incubation with active caspase-3, and nearly 99% of ROS-LNPs was cleaved to free DOX within 4 h, indicating the fast caspase-3-specific cleavage of DEVD-DOX (Fig. 1g and h).

The release behavior of ROS-LNPs was compared with free DOX and DEVD-DOX in PBS at 37 °C (Fig. 1i). As expect, free DOX was rapidly released from 12 kDa dialysis membrane, with nearly complete release within 6 h. And, DEVD-DOX showed a moderately sustained release within 48 h, compared to free DOX, but it was completely released after 48 h. In contrast, ROS-LNPs provided a prolonged and controlled release for up to 48 h, wherein only 50% of ROS-NPs were released from 12 kDa dialysis membrane after 48 h, indicating that DEVD-DOX was very stably encapsulated into LNPs. Finally, the caspase-3-dependent cytotoxicity of ROS-LNPs was validated *in vitro* (Fig. 1j). When 4 T1 TNBC cells were treated with ROS-LNPs in the presence of caspase-3, dose-dependent cytotoxicity was observed, with an $IC_{50}$ value of 1.78 μM, which was comparable to that of free DOX (1.68 μM). In contrast, ROS-LNPs alone exhibited negligible cytotoxicity under the same. Conditions, confirming caspase-3-specific activation. Moreover, co-treatment of ROS-LNPs, caspase-3 (12.5 μg/mL), and caspase-3 inhibitor (12.5 μg/mL) greatly reduced the cytotoxic response of ROS-LNPs, further establishing that caspase-3-specific cleavage of DEVD-DOX in

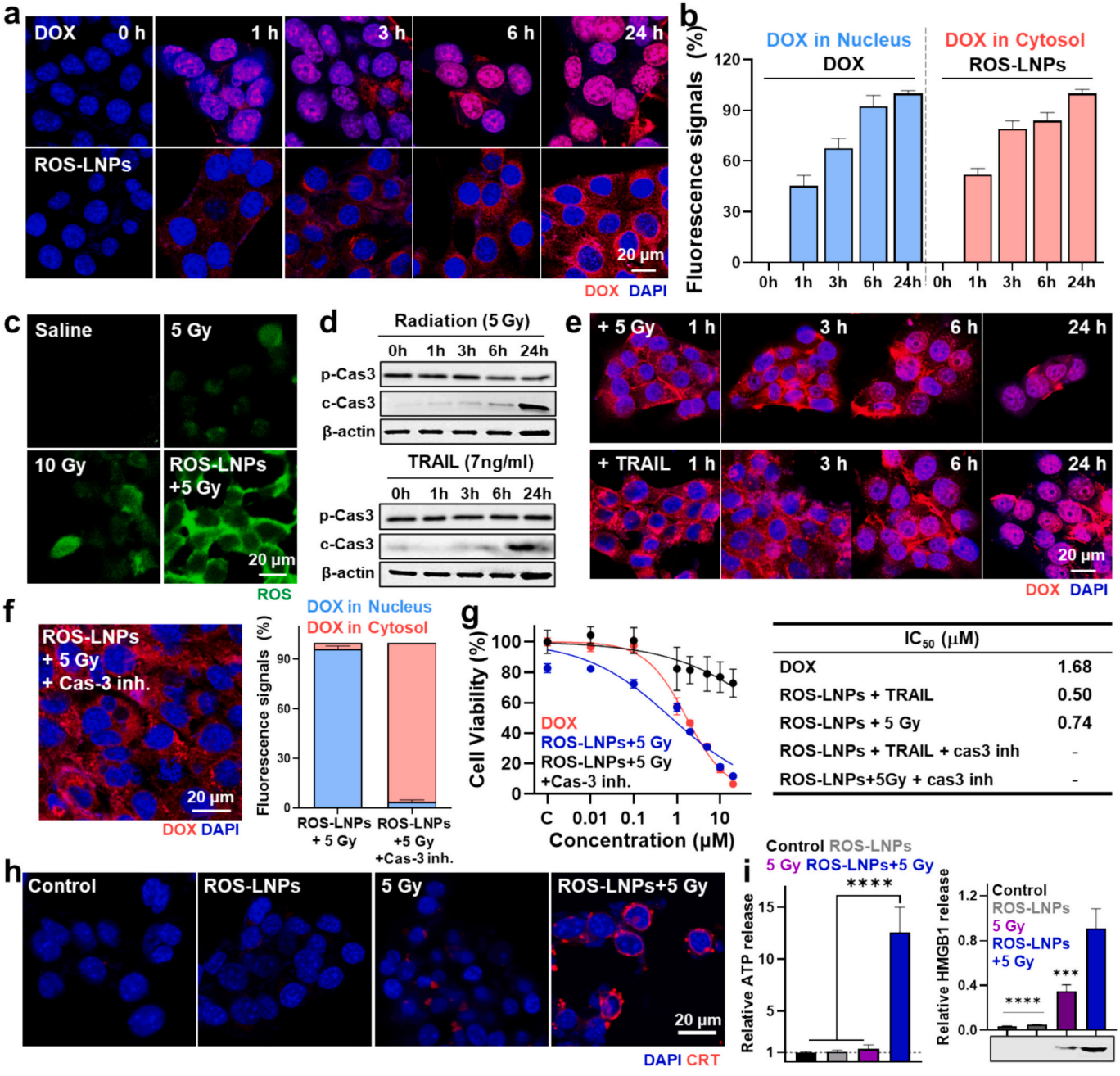


**Fig. 2.** ***In vitro*** **caspase-3-dependent drug activation and induction of ICD.** (a) CLSM images of the time-dependent cellular uptake and localization of free DOX (2 μM) and ROS-LNPs (2 μM, based on DOX) in 4 T1 cells. (b) Quantitative fluorescence analysis of nucleus and cytosolic DOX distribution. (c) ROS generation (d) Western blot analysis of cleaved caspase-3 expression in 4 T1 cells following treatment with low-dose radiation (5 Gy) or TRAIL (7 ng/mL). (e) CLSM images and quantitative distribution of DOX in 4 T1 cells treated with ROS-LNPs (2 μM, based on DOX) after caspase-3 activation by low-dose radiation (5 Gy) or TRAIL (7 ng/mL). (f) CLSM images demonstrating the inhibition of caspase-3-mediated DOX release using caspase-3 inhibitor (12.5 μg/mL). (g) Cell viability and corresponding $IC_{50}$ values of 4 T1 cells across different treatment groups for 24 h. (h) Representative CLSM images illustrating the cell surface exposure of CRT. (i) Quantitative analysis of relative ATP and HMGB1 release as DAMPs. In (b, d, f, h), data are presented as the mean ± SD (n = 3). Significance was determined by one-way analysis of variance (ANOVA) followed by Tukey-Kramer post-hoc tests (***$p < 0.001$, ****$p < 0.0001$).

LNPs essential for prodrug activation mechanism in physiological conditions.

### 2.2. ROS-activable cytotoxicity and ICD of ROS-LNPs in cell culture system

The cellular uptake and intranuclear localization of free DOX (2 μM) and ROS-LNPs (2 μM DOX-equivalent) were examined using 4 T1 TNBC cells (4 T1 cells), wherein both free DOX and ROS-LNPs were visualized using the confocal laser scanning microscopy (CLSM) (Fig. 2a**)**. As a control, free DOX (red color) was rapidly internalized by 4 T1 cells and mainly localized in the nucleus (blue color) within 24 h of incubation. This observation suggests that free DOX readily intercalates into nuclear DNA. Quantitative analysis of fluorescence signals at 1, 3, 6, and 24 h demonstrated that intracellular accumulation of free DOX progressively increased over time, whereas ROS-LNPs exhibited a time-dependent increase in fluorescence that remained confined to the cytoplasm without translocation into the nucleus **(**Fig. 2b**)**. In the absence of caspase-3 in live cancer cells, DEVD-DOX released from ROS-LNPs maintained a bulky prodrug form that prevented the nuclear membrane permeation of DEVD-DOX, indicating that DEVD-DOX remained in an inactive form within the cytoplasm of 4 T1 cells.

To determine whether ROS generated by low-dose radiation activates caspase-3, 4 T1 cells were treated with low-dose radiation (5Gy). This dose was selected because radiation-induced ROS responses have been reported even at 1–5 Gy, and the fraction of ROS-producing cells increased as the dose escalated within the low-Gy range. This dose dependence could accelerate caspase-3-mediated activation of ROS-LNPs. Therefore, 5 Gy was chosen as a practical upper-end low-dose condition that maximizes ROS-dependent triggering while avoiding the pronounced intrinsic cytotoxicity observed at higher doses [44,45]. It is known that radiation induces cell death primarily through DNA damage and ROS generation, leading to apoptosis *via* the intrinsic mitochondrial pathway [46,47]. This process activates caspase-3 that is the primary executioner enzyme in apoptosis, responsible for the final morphological and biochemical changes [48,49]. To evaluate radiation-dependent ROS generation, intracellular ROS levels were measured with DCFH-DA assay in 4 T1 cells treated with saline, 5 Gy, or 10 Gy dose intensity. The amount of ROS generation (green color) increased in proportion to the radiation dose from 5 Gy to 10 Gy, indicating that low-dose radiation successfully generated sufficient amounts of ROS in cell culture system (Fig. 2c **and S5**). As control, no ROS generation is observed in saline-treated cancer cells. Importantly, when the cancer cells were treated with ROS-LNPs and 5 Gy dose radiation, the highest ROS generation (green color) was clearly observed, representing approximately 10.1- and 5.6-fold increases compared to the 5 Gy and 10 Gy radiation groups, respectively. These results indicate that the free DOX cleaved by active caspase-3 further generated large amounts of ROS in culture system, whereas ROS-LNPs alone did not induce any detectable ROS generation. Western blot analysis revealed that the expression of active caspase-3 increased after 3 h post-radiation with 5 Gy dose intensity and large amount of caspase-3 was clearly observed after 24 h (Fig. 2d **and S6**). As control, similar caspase-3 activation was observed when 4 T1 cells were also treated with TRAIL (7 ng/ml), a well-known cell apoptosis inducer. Next, in order to determine whether ROS-induced caspase-3 activation could trigger the cleavage of DEVD-DOX released from ROS-LNPs, 4 T1 cells were incubated with ROS-LNPs (2 μM DOX-equivalent) for 24 h, followed by treatment with 5 Gy radiation or TRAIL (7 ng/ml) for 24 h (Fig. 2e **and S7**). As we expect, the time-dependent nuclear localization of free DOX from ROS-LNPs were clearly observed in 5 Gy radiation- or TRAIL-treated 4 T1 cells. In both cases, cytosol-accumulated DEVD-DOX released from ROS-LNPs was cleaved by caspase-3 activated by the subsequent 5 Gy radiation-generated ROS or TRAIL treatment and the cleaved DOX molecules gradually translocated into the nucleus from 1 h to 6 h. After 24 h post-low-dose radiation or TRAIL treatment, most free DOX molecules were mainly observed in the nucleus in 4 T1 treated with low-dose radiation or TRAIL treatment. This was because TRAIL or low-dose radiation increased intracellular ROS during apoptosis. Elevated ROS could disrupt lipid membranes and increase membrane permeability [50,51]. As a result, a fraction of DEVD-DOX became cytosol-accessible, allowing active caspase-3 to cleave the DEVD linker and release free DOX. In contrast, when 4 T1 cells were pretreated with both ROS-LNPs and irreversible caspase-3 inhibitor (12.5 μg/mL) for 24 h, they did not show any cleavage of DEVD-DOX after low-dose radiation for 24 (Fig. 2f). This is because most DEVD-DOX released from ROS-LNPs in caspase-3 inhibitor-pretreated 4 T1 cells mainly localized in cytoplasm even with low-dose radiation. Following caspase-3 inhibitor treatment, which inhibits the activity of caspase-3, the fluorescence signals of DEVD-DOX in the nucleus of low-dose radiation treated 4 T1 cells was significantly reduced by 96.8% compared to the 4 T1 cells treated with ROS-LNPs and low-dose radiation.

*In vitro* experiments confirmed that the cytotoxicity of ROS-LNPs greatly depends on the caspase-3 activation induced by low-dose radiation (Fig. 2g **and Fig. S8**). When 4 T1 cells were treated with free DOX or ROS-LNPs + low-dose radiation (5 Gy), the dose-dependent cytotoxicity of free DOX and ROS-LNPs was clearly observed. The $IC_{50}$ of ROS-LNPs +5 Gy radiation was 0.74 μM, 2.27-fold lower than that of free DOX (1.68 μM) in 4 T1 cells. This result indicated that the low-dose radiation generating ROS can activate the cytotoxicity of ROS-LNPs *via* caspase-3-activataible cell death mechanism. Furthermore, ROS-LNPs showed the higher cytotoxicity compared to free DOX upon low-dose radiation, suggesting cleaved DOX molecules further amplify the cytotoxicity of ROS-LNPs. As control, the $IC_{50}$ of ROS-LNPs with TRAIL-pretreated 4 T1 cells was measured to 0.5 μM, 3.34-fold lower than that of free DOX. These results suggest that caspase-3 activation induced by low-dose radiation or TRAIL is sufficient to induce the caspase-3-activatable cytotoxicity of ROS-LNPs in cell culture system. In contrast, co-treatment of ROS-LNPs with a caspase-3 inhibitor greatly reduced the cytotoxicity even with low-dose radiation or TRAIL, further establishing that active caspase-3-induced cleavage of DEVD peptide linker of prodrug is essential for the ROS-activatable cytotoxicity mechanism of ROS-LNPs. Finally, the immunogenic cell death (ICD) of ROS-LNPs was evaluated by measuring damage-associated molecular patterns (DAMPs) in 4 T1 cells (**Fig. 2h** and **i**). As control, saline- and ROS-LNPs-treated groups did not exhibit detectable DAMPs. 5 Gy radiation alone induced a slight increase in DAMPs, such as Calreticulin (CRT) and HMGB1. In particular, the combination of ROS-LNPs+5 Gy radiation significantly enhanced the ICD signals. Specifically, the CRT surface exposure in the ROS-LNPs+5 Gy group was 7.62-fold higher than that of 5 Gy radiation group (**Fig. S9**). Furthermore, ATP release and HMGB1 secretion of ROS-LNPs+5 Gy radiation were 9.2-fold and 3.3-fold higher, respectively, compared to 5 Gy radiation group. These results demonstrated that ROS-LNPs with 5 Gy radiation effectively induce ICD in cell culture system. Overall, these findings suggest that low-dose radiation generates a sufficient level of ROS to trigger the apoptotic cascade *via* caspase-3 activation. In this system, the activated caspase-3 subsequently cleaves DEVD-DOX released from ROS-LNPs, fallowing free DOX further amply the ROS-induced apoptosis and ICD of ROS-LNPs to effectively eradicate cancer cells.

### 2.3. MSC-mediated enhanced intratumoral accumulation of ROS-LNPs

To ensure the uniform and sustained delivery of ROS-LNPs into tumor tissues, previously developed implantable micro-syringe chip (MSC) containing drug reservoir and microfluid channel was meticulously constructed *via* photolithographic techniques (Fig. 3a **and S10**) [36]. The resulting MSC had a size of 10.0 × 3.7 × 0.1 mm (height × width × thickness) and could stably contain 2 μL of drug solution in internal drug reservoir. The TEM image confirmed the presence of 1) 1 mm inlet of drug reservoir and 2) ten 50 μm outlet micro-holes at the tip of the needle (Fig. 3b). Because MSC was fabricated from biocompatible PSA, the device remained safe for long-term implantation *in vivo* [52].

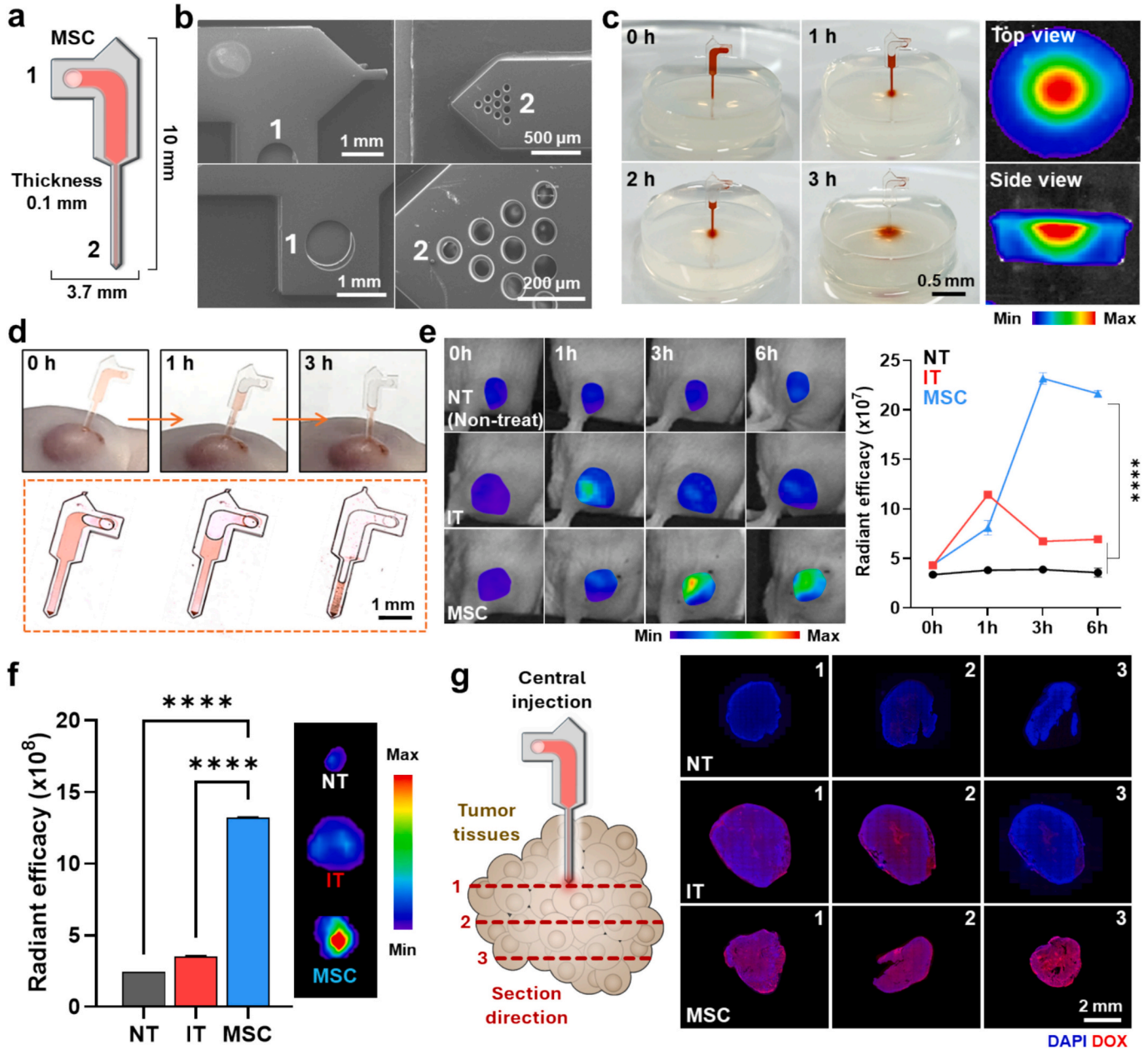


**Fig. 3.** ***In vivo*** **evaluation of tumor accumulation and distribution** ***via*** **MSC injection.** (a) Schematic illustration of MSC. (b) TEM images showing the inlets and outlets of the micro-hole array on the fabricated MSC. (c) Time-lapse monitoring of sustained drug release and uniform spatial distribution of ROS-LNPs (32 mg/mL, based on DOX) within an agarose gel, including top- and side-view fluorescence images. (d) Representative images illustrating the MSC implantation procedure in a 4 T1 tumor-bearing mouse. (e) *In vivo* NIRF imaging and quantitative analysis of 4 T1 tumor-bearing mice (n = 3) over 6 h comparing IT and MSC-mediated administration of ROS-LNPs (0.8 mg/kg, based on DOX). (f) *Ex vivo* fluorescence images and quantitative accumulation of ROS-LNPs in excised tumor tissues at 6 h post-injection. (g) Schematic of tumor sectioning location and CLSM images showing the spatial and homogeneous distribution of ROS-LNPs *via* MSC-mediated administration. In (e, f), data are presented as the mean ± SD (n = 3). Significance was determined by one-way analysis of variance (ANOVA) followed by Tukey-Kramer post-hoc tests (****$p < 0.0001$).

Furthermore, the needle length exceeded 5 mm, which allowed for the effective delivery of ROS-LNPs into deep tumor regions. Prior to *in vivo* application, the discharge profile of ROS-LNPs released from the MSC was evaluated through agarose gel (Fig. 3c). After loading 2 μL of ROS-LNPs (32 mg/mL, based on DOX) dissolved saline solution into the drug reservoir, the red color of ROS-LNPs was completely released within 3 h and exhibited a uniform fluorescent distribution that originated from the outlet position of MSC after 3 h post-injection.

Next, the tumor accumulation of ROS-LNPs was investigated in breast tumor-bearing mice, which are prepared by subcutaneous inoculation of 4 T1 cells ($1 \times 10^6$) into left flank of balb/c nude mice ($n = 3$). When the tumor volumes were approximately 200 ± 10 $mm^3$, the ROS-LNPs (0.8 mg/kg, based on DOX)-loaded MSC was intratumorally implanted after a small pinhole was created on the skin using a 26 G stainless steel needle (Fig. 3d). The MSC device discharged 63 ± 2.2% of the loaded drug solution smoothly into tumor tissues, and no significant leakage or reflux was observed [36]. Throughout the 3 h injection period, the MSC-mediated intratumoral delivery system demonstrated sufficient mechanical toughness and flexibility to prevent needle breakage. This MSC-mediated delivery system allowed the ROS-LNPs to be precisely injected to the center of the tumor tissue with minimal invasiveness. Conventional intratumoral (IT) injection using a 26 G

stainless steel needle was employed as a comparative control to evaluate the accumulate efficiency. After injecting ROS-LNPs through two administration routes, the biodistribution and accumulation in tumor tissues were observed over 6 h using *in vivo* imaging system (IVIS) (Fig. 3e). In the case of IT injection, ROS-LNPs was accumulated in the tumor more rapidly than MSCs but also exhibited faster clearance. In contrast, MSC-mediated delivery provided a sustained release of ROS-LNPs, allowing gradual diffusion into the tumor tissue and resulting in peak tumor accumulation at 3 h post-injection. When the maximal tumor accumulation was reached at 3 h, the fluorescence signal of ROS-LNPs in tumor tissues with MSC-mediated injection was 3.26-fold brighter than that in tissues with IT injection, respectively. The lower accumulation of ROS-LNPs in tumor tissues following IT injection was attributed to the rapid leakage of the injected ROS-LNPs into surrounding normal tissues, driven by transient intratumoral pressure. This phenomenon likely occurs because IT injected ROS-LNPs can be quickly cleared *via* blood and lymphatic vessels before achieving uniform dispersion and cellular uptake.

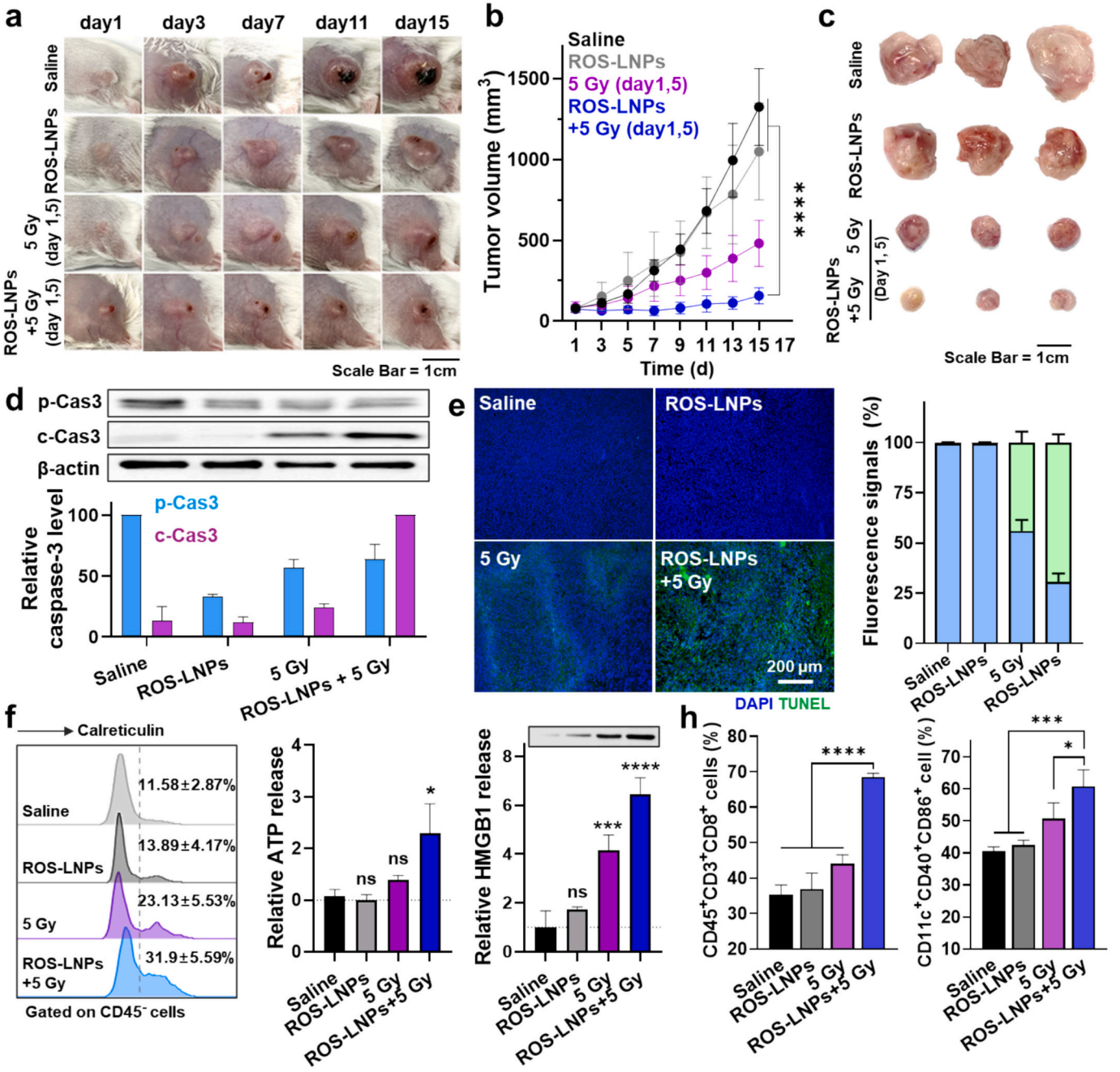


**Fig. 4.** ***In vivo* therapeutic efficacy of ROS-LNPs and induction of ICD.** (a) Representative digital photographs of 4 T1 tumor-bearing mice monitored over 15 days following four different treatments: (i) Saline, (ii) ROS-LNPs (0.8 mg/kg, based on DOX), (iii) 5 Gy radiation, and (iv) ROS-LNPs+5 Gy. (b) Average tumor growth curves of 4 T1 tumor-bearing mice monitored throughout the 15-day treatment period. (c) Digital photographs of excised tumors harvested at the end of the experiment. (d) Western blot analysis of pro-caspase-3 and cleaved caspase-3 expression levels in excised tumor tissues. (e) Representative fluorescence images and quantitative analysis of the apoptotic cell population in TUNEL-stained tumor sections. (f) Representative flow cytometric histograms of CRT-positive tumor cells gated on $CD45^-$ cells and extracellular release of HMGB1 and ATP in tumor supernatants. (h) Quantitative flow cytometric analysis of tumor-infiltrating $CD8^+$ T cells ($CD45^+CD3^+CD8^+$) and matured dendritic cells ($CD11c^+CD40^+CD86^+$). In (b, d, e, f, h), data are presented as the mean ± SD ($n = 5$). Significance was determined by one-way analysis of variance (ANOVA) followed by Tukey-Kramer post-hoc tests (ns = no significance, $^*p < 0.05$, $^{***}p < 0.001$, $^{****}p < 0.0001$).

In addition, the *ex vivo* fluorescence imaging of excised tumor tissues further demonstrated that MSC-mediated injection of ROS-LNPs resulted in 3.4-fold higher tumor accumulation compared to IT injection after 6 h post-injection (**Fig. 3f**). The excised tumor tissues were sampled from three different locations and further observed in precision using CLSM to examine the intratumoral distribution of ROS-LNPs (**Fig. 3g**). In Sections 1 and 2, both IT and MSC injection enabled delivery of ROS-LNPs into the tumor tissue. However, as shown in Section 3, ROS-LNPs were no longer detectable in the IT injection group, whereas MSC-mediated injection maintained detectable levels within the tumor tissue. Moreover, MSC-mediated injection of ROS-LNPs facilitated more homogeneous intratumoral distribution and thereby enhanced overall delivery efficiency. These results indicate that MSC-mediated injection facilitates prolonged retention and enhances the spatial distribution of ROS-LNPs. As shown by *ex vivo* near infrared fluorescence (NIRF) imaging, IT injection resulted in significantly higher accumulation in the kidney and liver after 6 h post-injection (kidney: 1.4 -fold; liver: 1.3 -fold) compared with the MSC injection (**Fig. S11**). This observation likely reflects a limitation of IT administration, namely the rapid leakage of injected ROS-LNPs into surrounding normal tissues. From a translational perspective, clinical implementation of MSC-mediated intratumoral infusion may face several practical hurdles, in particular ensuring consistent and precise placement of the delivery system within heterogeneous human tumors. This limitation could be mitigated by integrating the procedure with established image-guided interventions, where ultrasound or CT guidance has been used to place and retrieve intratumoral microdevices at clinically relevant depths, improving placement accuracy and procedural reproducibility [53].

### 2.4. In vivo therapeutic efficacy of ROS-LNPs in tumor xenograft mouse models

Following confirmation of the tumor targeted delivery efficiency of MSC-mediated ROS-LNPs injection, the therapeutic efficiency of low-dose radiation generated ROS-activatable ROS-LNPs in TNBC treatment was evaluated (Fig. 4a). When tumors in 4 T1-xenografted BALB/c mice reached 80 ± 20 $mm^3$, mice were randomly divided into 4 groups ($n = 5$); (i) Saline, (ii) ROS-LNPs (0.8 mg/kg, based on DOX), (iii) Low-dose radiation (5 Gy), (iv) ROS-LNPs (0.8 mg/kg, based on DOX) + Low-dose radiation (5 Gy), respectively. ROS-LNPs were loaded into MSC and implanted center of the tumor tissues for 3 h and the tumor tissues were then exposed to 5 Gy after the 1st and 5th day of ROS-LNPs administration (**Fig. S12**). As control, following the high-dose radiation with 10 Gy in 4 T1 tumor-bearing mice, rapid weight loss was observed and two mice died within 15 days, revealing severe systemic toxicity, so only low-radiation with 5 Gy was studied in animal studies (**Fig. S13**). Although 5 Gy radiation treatment is not enough to generate ROS that completely eradicate aggressive tumor tissues, it can be mainly used to activate caspase-3, which can activate ROS-LNPs in tumor tissues, while avoiding the severe toxicity associated with high-dose radiation. After 15 days post-treatment, ROS-LNPs +5 Gy (145 ± 51 $mm^3$) group exhibited significant inhibition of tumor growth, compared to saline (1324 ± 237 $mm^3$), ROS-LNPs (1047 ± 299 $mm^3$), and 5 Gy radiation (480 ± 143 $mm^3$) groups, respectively (Fig. 4b **and S14)**. As we expect, ROS-LNPs treatment did not show any therapeutic efficacy, due to the low expression level of caspase-3 in tumor tissues without low-dose radiation. In the ROS-LNPs + low-dose radiation groups, tumor volumes decreased by approximately 9.1-, 6.6-, and 3.3-folds compared to the saline, ROS-LNPs, and 5 Gy radiation groups, respectively. After 15 days post-treatment, excised tumor images visually confirmed the significant tumor suppression in the ROS-LNPs +5 Gy group (Fig. 3c). The morphology of all groups was highly consistent with the quantitative volume data, demonstrating the high reproducibility of all treatments. From these results, the combination of ROS-LNPs and low-dose radiation showed improved therapeutic efficacy, wherein low-dose radiation generated ROS can activate ROS-LNPs in targeted tumor tissues and the activated DOX can further amplify the cancer cell death in targeted tumor tissues.

We further evaluated caspase-3 expression in tumor tissues by western blotting (**Fig. 4d**). For this analysis, mice from all treatment groups were sacrificed on day 15 post-treatment, and tumor tissues were harvested for protein extraction. No expression of active caspase-3 was observed in saline- and ROS-LNPs-treated tumor tissues. However, an increased level of active caspase-3 was clearly observed in the group treated with low-dose radiation, indicating that low-dose radiation can generate enough ROS to activate caspase-3 in tumor tissues. Importantly, ROS-LNPs +5 Gy radiation treatment showed the notable increased expression level of caspase-3, due to the amplified cell death mechanism of ROS-LNPs with low-dose radiation. The expression level of caspase-3 of ROS-LNPs +5 Gy low-dose radiation treated tumor tissues was 7.6-, 8.2-, and 4.1-fold higher than that in tumor tissues with the saline, ROS-LNPs, and 5 Gy radiation treatment, respectively. TUNEL staining revealed that the ROS-LNPs +5 Gy radiation induced extensively widespread cell death throughout the tumor tissue rather than being confined only to the initial radiation sites (Fig. 4e). This outcome was driven by a potent apoptosis amplification mechanism, in which the ROS-induced activated caspase-3 successfully activated DEVD-DOX molecules released from ROS-LNPs that are homogeneously distributed in whole area of tumor tissues, following free DOX molecules further induced a amplified apoptosis of ROS-LNPs without low-dose radiation. As a result, the initial localized cell death by low-dose radiation was effectively converted into a tumor-wide therapeutic response of ROS-LNPs and resulted in approximately 25% greater apoptotic activity, compared to low-dose radiation alone. In addition, DAB staining of cleaved caspase-3 revealed that the ROS-LNPs +5 Gy group exhibited significantly more widespread caspase-3 activation compared to the low-dose radiation treatment alone (**Fig. S15**). Furthermore, H&E staining demonstrated robust histological signs of apoptosis through marked morphological changes, which strongly supports and reinforces the interpretation of the TUNEL results.

Next, we investigated the antitumor immune responses by measuring DAMPs from tumor tissues. The proportion of CRT-positive tumor cells ($CD45^-CRT^+$; 31.9 ± 5.59%) within tumor tissues was significantly higher than that observed in saline (11.58 ± 2.87%), ROS-LNPs (13.89 ± 4.17%), and 5 Gy radiation (23.13 ± 5.53%) groups. In addition, the extracellular release of HMGB1 and ATP into the tumor supernatants were significantly increased in ROS-LNPs +5 Gy radiation group, showing approximately 6.4-fold and 2.3-fold increases, respectively, compared with other groups (Fig. 4f). The induction of DAMPs promoted an immunogenic shift in the tumor microenvironment, resulting in enhanced immune activation. Specifically, the population of $CD8^+$ T cells in the ROS-LNPs +5 Gy group was 1.94-, 1.86-, and 1.56-fold higher than those in the saline, ROS-LNPs, and 5 Gy groups, respectively (Fig. 4h). Similarly, the proportion of $CD86^+$ matured dendritic cells showed 1.5-, 1.43-, and 1.20-fold increases relative to the same respective groups, showing enhanced immunity. These findings demonstrate that ROS-LNPs leverage radiation-induced caspase-3 activation to initiate an amplified apoptotic cascade that extends beyond the initial radiation site. This process triggers potent immunogenic cell death signaling and subsequent robust immune activation, ultimately leading to significantly enhanced antitumor effects. Although immune modulation was demonstrated in the 4 T1 syngeneic setting, further evaluation in humanized mouse models bearing MDA-MB-231 tumors will further enhance the clinical relevance and translational significance of this approach [54].

### 2.5. In vivo safety of ROS-LNPs in 4 T1 tumor bearing mice

The *in vivo* safety of ROS-LNPs in combination with low-dose radiation was evaluated in 4 T1 tumor-bearing mice ($n = 5$). No significant body weight loss or histopathological damage to major organs was observed in the saline, ROS-LNPs, 5 Gy, and ROS-LNPs +5 Gy radiation

groups at day 15 post-treatment (Fig. 5a **and Fig. S16)**. This high level of biocompatibility is likely due to the fact that the DOX dosage used (0.8 mg/kg) is remarkably lower than standard therapeutic levels. For instance, conventional intravenous (IV) administration of DOX typically requires 1–5 mg/kg in murine models [55]. As we expect, blood analyses showed that hematological parameters in 4 T1 tumor-bearing mice, including blood urea nitrogen (BUN), alanine transaminase (ALT), aspartate aminotransferase (AST), and neutrophils (Neu), remained within the normal range following repeated systemic administration of ROS-LNPs+5 Gy **(**Fig. 5b**)**. No significant differences were observed compared with the Saline group, indicating that MSC administration with low dose radiation did not induce systemic toxicity. The histological analysis of normal organs was further carried out upon completing the therapy and monitoring, discovering that all normal organs from ROS-LNPs+5 Gy treated mice were preserved with their normal integrities without any remarkable damage similar to saline-treated ones due to the inactiveness of ROS-LNPs inside the normal tissues with low capase-3 levels **(**Fig. 5c**)**. These findings demonstrate that combination therapy with ROS-LNPs and low-dose radiation can effectively mitigate the off-target toxicity typically associated with anticancer drugs.

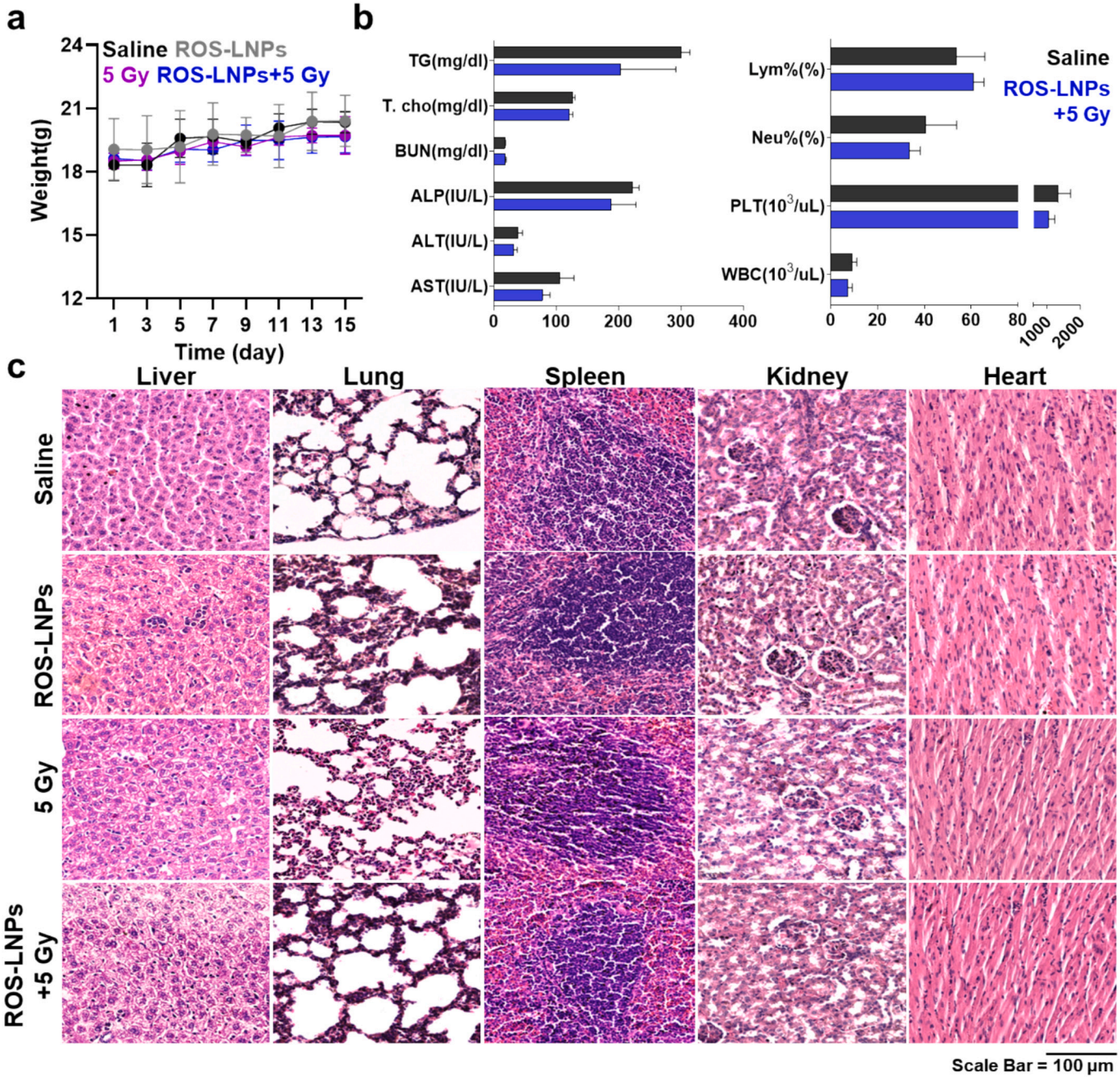


**Fig. 5.** ***In vivo*** **biocompatibility of ROS-LNPs.** (a) Body weight changes of 4 T1 tumor-bearing mice monitored over 15 days post-treatment in four groups: (i) Saline, (ii) ROS-LNPs (0.8 mg/kg, based on DOX), (iii) 5 Gy radiation, and (iv) ROS-LNPs+5 Gy. (b) Comprehensive hematological and biochemical analysis of blood samples, including liver enzymes (ALT, AST, ALP), kidney function (BUN), and blood cell counts (WBC, PLT, Neu%, Lym%), comparing Saline and ROS-LNPs+5 Gy groups. (c) Representative H&Estained histological images of major organs (liver, lung, spleen, kidney, and heart) harvested at day 15 to evaluate off-target toxicity and organ integrity. In (a, b), data are presented as the mean ± SD (n = 5).

## 3. Conclusion

Current radiotherapeutic strategies for TNBC remain largely dependent on high-dose radiation to achieve sufficient tumor control. However, high-dose radiation is frequently accompanied by severe systemic toxicity and still fails to eradicate radioresistant tumor regions uniformly. Moreover, high-dose radiation primarily induces damage confined to the irradiated field, limiting its ability to address spatial heterogeneity within solid tumors without further increasing dose-related toxicity. In this work, we developed low-dose radiation generated ROS-activatable DOX prodrug-loaded liposome nanoparticles (ROS-LNPs) as a precision chemo-radiotherapeutic platform for TNBC. Instead of relying on high-dose radiation associated with severe systemic toxicity, our strategy exploited low-dose radiation (5 Gy) to induce localized ROS generation within tumor tissues, which initiates apoptosis and triggers the release of active caspase-3 in irradiated cancer cells. This initial, spatially confined apoptotic event functions as a biochemical trigger rather than a direct cytotoxic insult. The low-dose radiation-induced caspase-3 subsequently cleaved the DEVD linker of ROS-LNPs present in neighboring tumor regions, leading to localized release of free doxorubicin from adjacent ROS-LNPs. The released DOX then induced additional apoptosis in surrounding cancer cells, producing further caspase-3 and reinforcing ROS production, thereby establishing a sequential and self-propagating apoptotic cascade. Through this caspase-3 mediated amplification mechanism, spatially confined low-dose radiation was effectively converted into widespread tumor cell death that extends beyond the initially irradiated area, while maintaining minimal off-target toxicity. Beyond direct cytotoxicity, the amplified apoptotic process induced robust ICD, as evidenced by enhanced DAMPs release, dendritic cell maturation, and cytotoxic T-cell infiltration, thereby coupling apoptosis amplification with effective immune activation. Notably, this immune activation arose as a downstream consequence of amplified tumor apoptosis rather than from radiation dose escalation.

From a broader perspective, this work presented a conceptual shift from dose-escalation based radiotherapy to signal-amplified low-dose radiation therapy enabled by ROS-responsive nanomedicine. By decoupling therapeutic efficacy from high radiation doses, the ROS-LNP platform provided safer and mechanistically precise strategy to overcome radioresistance in aggressive tumors. The modular design of the caspase-responsive prodrug and liposomal carrier further allowed adaptability to other cytotoxic agents, alternative enzyme-responsive linkers, and diverse solid tumor types. Collectively, ROS-LNPs offer a versatile framework for next-generation chemoradiotherapy that integrates low-dose radiation, amplified apoptosis, and immune activation, highlighting their potential for translational application in drug-resistant and immunologically cold tumors.

## 4. Methods

### 4.1. Materials

Doxorubicin hydrochloride (DOX) was obtained from FutureChem (Seoul, Republic of Korea), and the p(Alloc)KGDEVD peptide was purchased from GL Biochem (Shanghai, China). 1-palmitoyl-2-oleoyl-sn-glycero-3-phosphocholine (POPC) was purchased from Avanti Polar Lipids (Alabaster, AL, USA), while cholesterol, phosphatidylserine (PS), acetonitrile (ACN), *N*,*N*-dimethylformamide (DMF), and chloroform were obtained from Sigma-Aldrich (St. Louis, MO, USA). Bis(4-nitrophenyl) carbonate (PABC) was acquired from TCI (Tokyo, Japan), methanol from Duksan (Republic of Korea), and ethyl ether from Daejung Chemicals (Republic of Korea). Recombinant human caspase-3 protein (cat# 707-C3/*CF*) and recombinant mouse TRAIL protein (cat# 1121-TL) were supplied by R&D Systems (Minneapolis, MN, USA), and the caspase-3 inhibitor *Z*-DEVD-FMK (cat# HY-12466) was obtained from MedChemExpress (Monmouth Junction, NJ, USA). The caspase-3 antibody (cat# 9661 L) was obtained from Cell Signaling Technology (Danvers, MA, USA). Recombinant anti-calreticulin antibody conjugated with Alexa Fluor® 647 (cat# ab196159) was purchased from Abcam (Cambridge, United Kingdom). Fluorophore-conjugated antibodies against mouse CD45.2 (cat# 109828), CD8a (cat# 100712), CD3 (cat# 100218), CD11c (cat# 117310), CD40 (cat# 124610), CD86 (cat# 105006), and red blood cell lysis buffer (Cat#: 420301) were commercially available from BioLegend (San Diego, CA, USA). The tumor dissociation kit was purchased from Miltenyi Biotec (Bergisch Gladbach, Germany), and FcBlock™ was purchased from BD (BD, New Jersey, USA). A monoclonal anti-mouse β-actin antibody and a hematoxylin and eosin (H&E) staining kit were acquired from Abcam (Gyeonggi-do, Republic of Korea), and 4′,6-diamidino-2-phenylindole (DAPI) was purchased from Thermo Fisher Scientific (Waltham, MA, USA). The TUNEL assay kit was purchased from Promega (Madison, WI, USA), and the Quanti-Max™ WST-8 cell-viability kit was obtained from BIOMAX (Gyeonggi-do, Republic of Korea). RPMI-1640 medium and fetal bovine serum were supplied by Welgene (Gyeongsangbuk-do, Republic of Korea), and antibiotics were acquired from GenDEPOT (Katy, TX, USA). 4 T1 murine mammary carcinoma cells were obtained from the American Type Culture Collection (ATCC; Manassas, VA, USA), and five-week-old BALB/c were purchased from NaraBio (Seoul, Republic of Korea).

### 4.2. Instruments

The diameter, colloidal stability, and zeta potential of liposomes were characterized by dynamic light scattering (DLS; Zetasizer Nano ZS, Malvern Instruments, Worcestershire, UK). Liposome size and morphology were examined by cryogenic transmission electron microscopy (cryo-TEM; Thermo Scientific Glacios 2, Thermo Fisher Scientific, Waltham, MA, USA). The synthetic outcome and caspase-3-specific cleavage of KGDEVD-PABC-DOX were confirmed by reverse-phase high-performance liquid chromatography coupled to mass spectrometry (RP-HPLC/MS; 1260 Infinity II LC system, Agilent Technologies, Santa Clara, CA, USA) equipped with a C18 column. Cell viability was quantified using a microplate reader (Infinite M Nano, Tecan, Männedorf, Switzerland). *In vitro* cellular uptake fluorescence images were acquired by confocal laser scanning microscopy (CLSM; Zeiss LSM880 Airyscan, Carl Zeiss AG, Oberkochen, Germany) at the Ewha Fluorescence Core Imaging Center (NFEC-2016-05-209,580). *Ex vivo* tissue fluorescence images were obtained using a fluorescence microscope (EVOS M7000, Thermo Fisher Scientific, Waltham, MA, USA). Western blot signals for caspase-3 expression in cells and tissues were recorded with a Western blot imaging system (iBright CL750, Thermo Fisher Scientific, Waltham, MA, USA). *In vivo* and *ex vivo* whole-body and organ fluorescence imaging was performed using an *in vivo* imaging system (IVIS® Lumina III, PerkinElmer, Waltham, MA, USA) at the Ewha Drug Development Research Core Center. *In vivo* radiation therapy was delivered using a Leksell GammaPlan® (v. 11.4.2; Elekta AB, Stockholm, Sweden). *In vitro* irradiation for cell treatments was performed with an X-RAD 320 biological irradiator (Precision X-Ray Inc., North Branford, CT, USA).

### 4.3. Preparation of ROS-LNPs

The ROS-activatable prodrug, DEVD-DOX, was synthesized through a series of multi-step liquid-phase organic reactions, all of which were conducted at room temperature. Initially, pKGDEVD (1 g, 1.1 mmol) was dissolved in anhydrous DMF and was reacted with EEDQ (544 mg, 2.2 mmol) and PABA (271 mg, 2.2 mmol). The reaction mixture was stirred for 16 h at room temperature. To recover the intermediate, the resulting solution was precipitated into cold diethyl ether, which afforded pKGDEVD-PABA as a pale yellow powder. Next, pKGDEVD-PABA intermediate (1016 mg, 1 mmol) was activated with bis(4-nitrophenyl) carbonate (1525 mg, 5 mmol) in DMF in the presence of DIPEA (524

μL, 3 mmol). This mixture was stirred for 12 h at room temperature. The solution was then precipitated into cold ether to yield the activated pKGDEVD-PABC intermediate as a slightly yellow powder. Subsequently, pKGDEVD-PABC (962 mg, 0.82 mmol) and DOX·HCl (568 mg, 0.98 mmol) were dissolved in DMF and treated with DIPEA (768 μL, 4.4 mmol). The mixture was stirred for 12 h at room temperature and was subsequently precipitated into cold distilled water to obtain the protected prodrug, pKGDEVD-DOX, as a red solid. In the final step, the protective groups were removed to afford the active form. pKGDEVD-DOX (1278 mg, 0.81 mmol) was dissolved in a mixture of chloroform and acetic acid (49:1, *v/v*) and was subjected to $Pd(PPh_3)_4$ (2801 mg, 2.4 mmol) and NMM (4 ml) under vacuum conditions. The deprotection reaction was allowed to proceed for 6 h at room temperature. The crude product was purified *via* preparative HPLC to remove residual reagents and was then lyophilized to afford the final DEVD-DOX as a red powder. After that, sodium carbonate was added to obtain the salt form of the product, enhancing its solubility. Each step was monitored and confirmed by RP-HPLC/MS equipped with a C18 column, using a linear gradient of acetonitrile in 3′DW from 10:90 to 90:10 (*v/v*) over 30 min at 1.0 ml/min.

DEVD-DOX encapsulated liposomes were prepared by a thin-film hydration method. POPC, cholesterol, PS, and KGDEVD-PABC-DOX were mixed at a molar ratio of 72.2:5.64:10.86:11.28. Lipid components were dissolved in chloroform and KGDEVD-PABC-DOX was dissolved in methanol; the solutions were combined and evaporated at 45 °C under reduced pressure to form a thin lipid film. The film was hydrated with triple-distilled water (3DW) at 55 °C for 30 min. Particle size was controlled by membrane extrusion through polycarbonate track-etched membranes (pore sizes as indicated). The hydrodynamic diameter and zeta potential were measured DLS. Liposome morphology was examined by cryo-TEM.

### 4.4. Characterization of ROS-LNPs

The average particle size and zeta potential of ROS-LNPs (1 mg/mL, based on DOX) dispersed in saline were analyzed by DLS. The bilayer spherical-shaped morphology of ROS-LNPs (1 mg/mL, based on DOX) in DW was visualized using TEM. The colloidal stability of ROS-LNPs (1 mg/mL, based on DOX) in saline was evaluated by DLS at 37 °C over a period of 9 days. Encapsulation efficiency (EE) of DEVD-DOX in ROS-LNPs was quantified by HPLC. A calibration curve was generated by measuring the fluorescence signal of DEVD-DOX standards at known input amounts. ROS-LNPs were diluted to 1 mg/mL (based on DOX) and analyzed by HPLC to quantify the encapsulated DEVD-DOX against the calibration curve. EE was calculated by comparing the measured DEVD-DOX amount in ROS-LNPs to the initial DEVD-DOX input used during formulation.

Enzyme-specific prodrug cleavage was evaluated by incubating DEVD-DOX (1 mg/mL, based on DOX) and ROS-LNPs (1 mg/mL, based on DOX) in 50 mM HEPES buffer containing 1 mM EDTA and recombinant Caspase-3 (12.5 ng/mL) at 37 °C for 4 h. To confirm enzyme specificity, caspase-3 inhibitor (12.5 μg/mL) was pre-incubated with the sample before enzyme treatment. Reaction products were analyzed by RP-HPLC/MS equipped with a C18 column under a DW/ACN gradient.

To examine the release profile of DOX from ROS-LNPs, 1 mL of DEVD-DOX and ROS-LNPs (1 mg/mL based on DOX) were loaded into a dialysis membrane (MWCO: 12 kDa) and incubated with gentle stirring in 30 mL of saline under sink conditions at 37 °C for 48 h.

For cytotoxicity, 4 T1 cells were seeded at $3 \times 10^5$ cells per well in 96-well plates and incubated for 24 h. Cells were treated with free DOX or ROS-LNPs (0–20 μM DOX-equivalents) for 24 h. To evaluate enzyme-responsive cytotoxicity, cells were incubated with either caspase-3 (12.5 μg/mL) or a combination of caspase-3 (12.5 μg/mL) and caspase-3 inhibitor (12.5 μg/mL). In the inhibition group, caspase-3 inhibitor was pre-added and incubated at 37 °C for 2 h prior to other treatments. To assess cell viability, 10% CCK-8 solution was then added, and the cells were incubated at 37 °C. Absorbance was measured on a microplate reader (absorbance: 450 nm).

### 4.5. ROS-activable cytotoxicity and ICD of ROS-LNPs in cell culture system

To observe cellular uptake and intranuclear localization, 4 T1 cells ($3 \times 10^5$ cells/well) were seeded in 24-well plates and treated with free DOX (2 μM) or ROS-LNPs (2 μM, based on DOX) for 1, 3, 6, and 24 h. Following incubation, the cells were fixed with 4% paraformaldehyde for 15 min and the nuclei were stained with DAPI for CLSM visualization. For quantitative analysis of the fluorescence signals, Image-Pro Plus software (Media Cybernetics, Silver Spring, MD, USA) was used. To confirm caspase-3-mediated activation, the cells were pre-incubated with ROS-LNPs (2 μM, based on DOX) for 24 h and subsequently exposed to low-dose X-ray radiation (5 Gy) or TRAIL (7 ng/mL). X-ray radiation was performed using an X-RAD 320 biological irradiator operated at 300 kV and 12.50 mA for an exposure time of 180 s. The source-to-surface distance (SSD) was maintained at 65 cm, resulting in a dose rate of approximately 1.67 Gy/min. For the inhibition study, the caspase-3 inhibitor (12.5 μg/mL) was pre-added 2 h prior to the radiation or TRAIL treatment.

Intracellular ROS generation was evaluated in 4 T1 cells ($3 \times 10^5$ cells/well) across four experimental groups including 5 Gy, 10 Gy, ROS-LNPs (2 μM, based on DOX), and ROS-LNPs+5 Gy. For the combined treatment group, cells were treated with ROS-LNPs for 24 h. Thereafter, 40 μM DCFH-DA was added and incubated for 1 h, followed by exposure to X-ray radiation (5 Gy). The resulting ROS levels were visualized and analyzed using an EVOS fluorescence microscope ($\lambda_{ex} = 504$ nm, $\lambda_{em} = 524$ nm).

For western blot analysis, 4 T1 cells ($3 \times 10^5$ cells/well) were harvested at the indicated times post-treatment. Total proteins were extracted using RIPA buffer containing protease and phosphatase inhibitor cocktails. The protein concentration was determined *via* BCA assay. Equal amounts of protein were separated by SDS-PAGE and transferred to PVDF membranes. The membranes were blocked with 5% BSA in TBS-T for 1 h and incubated with primary antibodies against procaspase-3, cleaved caspase-3, and β-actin overnight at 4 °C. After washing, the membranes were incubated with HRP-conjugated secondary antibodies for 1 h at room temperature and visualized using an ECL detection system. The band intensities were quantified using ImageJ software (NIH, Bethesda, MD, USA).

The enzyme-responsive cytotoxicity was determined by the CCK-8 assay. 4 T1 cells ($3 \times 10^3$ cells/well) were treated with ROS-LNPs (0–20 μM based on DOX) for 24 h, followed by treatment with 5 Gy radiation, 5 Gy + caspase-3 inhibitor (12.5 μg/mL), TRAIL (7 ng/mL), or TRAIL (7 ng/mL) + caspase-3 inhibitor (12.5 μg/mL). For groups involving the inhibitor, caspase-3 inhibitor was pre-added 2 h prior to the main treatment. After the specified incubation, 10% CCK-8 solution was added and measured using a microplate reader (absorbance: 450 nm).

To assess ICD induction, DAMPs were analyzed following the synergistic treatment of ROS-LNPs and RT. Surface-exposed CRT was quantified by flow cytometry; briefly, cells were harvested, incubated with an anti-CRT primary antibody at 4 °C for 1 h, followed by a fluorophore-conjugated secondary antibody for 30 min in the dark, and analyzed using a flow cytometer. Extracellular ATP release and HMGB1 secretion in the cell culture supernatants were measured using a luciferase-based ATP assay kit and an HMGB1 ELISA kit, respectively, according to the manufacturer's protocols. All immunological data were analyzed using FlowJo software.

### 4.6. In vivo biodistribution and intratumoral localization of ROS-LNPs

To evaluate the diffusion-mediated spatial distribution of the ROS-LNPs within a tissue-mimicking environment, an agarose gel

distribution assay was performed. A 1.0% (*w/v*) agarose gel was prepared to serve as a tumor phantom and ROS-LNPs (8 mg/mL, based on DOX) loaded MSC was carefully inserted into the center of the gel structure. To quantify and visualize the extent of drug distribution over time, the fluorescence signals derived from the ROS-LNPs were measured and analyzed using the IVIS Lumina III system.

For the *in vivo* biodistribution study, five-week-old female BALB/c mice (NARA Biotech, Seoul, Republic of Korea) were subcutaneously inoculated with $1 \times 10^6$ 4 T1 cells into the left flank. When the tumor volumes reached approximately $200 \pm 10$ $mm^3$, the mice were randomly assigned to control, IT and MSC groups. In the IT group, ROS-LNPs (0.8 mg/kg, based on DOX) were administered *via* a direct intratumoral injection as a single bolus using a 26 G syringe. For the MSC group, a guide hole was initially established in the tumor tissue using a 26 G needle followed by the insertion of ROS-LNPs (0.8 mg/kg, based on DOX) MSC for 3 h and immediately removed from the tumor.

Whole-body fluorescence imaging was conducted with an IVIS Lumina III system at pre-dose, 1 h, 3 h and 6 h post-dose to track the DOX-derived fluorescence. The intensity within the regions of interest was quantified using Living Image Software. At 6 h post-administration, the mice were sacrificed and the tumor as well as major organs (liver, lung, spleen, kidney, and heart) were excised for *ex vivo* imaging. For histological analysis, the excised tumors were embedded in OCT compound and cryo-sectioned at a thickness of 10 μm. The sections were stained with DAPI for 10 min and visualized using an EVOS M7000 fluorescence microscope to evaluate the spatial distribution and accumulation of the drug within the tumor tissue.

### 4.7. In vivo therapy

To establish the tumor model, $1 \times 10^6$ 4 T1 cells were subcutaneously inoculated into the left flank of five-week-old female BALB/c mice. When the tumor volumes reached $80 \pm 20$ $mm^3$, the mice were randomly assigned to four groups consisting of Saline, ROS-LNPs, 5 Gy, and ROS-LNPs+5 Gy. On Days 1 and 5, the MSC was inserted into the tumor, and 2 μL of ROS-LNPs (0.8 mg/kg, based on DOX) was administered over 3 h. For the groups receiving irradiation, a single dose of 5 Gy was delivered using a Gamma Knife for precise stereotactic treatment. Tumor volumes were measured every 2 days and calculated as (long axis) × (short axis)$^2$ × 0.53.

Excised tumors and major organs (liver, lung, spleen, kidney, and heart) were fixed in 4% paraformaldehyde and sectioned at a thickness of 10 μm. Tissue architecture and systemic toxicity were evaluated *via* H&E staining. Intratumoral apoptosis was assessed using the DeadEnd Fluorometric TUNEL System and caspase-3 immunohistochemistry with an anti-caspase-3 antibody and DAB substrate. All histological and fluorescence images were captured using an EVOS M7000 microscope and quantified with Image-Pro Plus software.

To investigate the induction of immunogenic cell death, extracellular ATP and HMGB1 levels in the tumor supernatants were measured using commercial ELISA kits while surface CRT expression was analyzed by flow cytometry. For the analysis of immune cell infiltration, tumors were dissociated into single-cell suspensions using a Tumor Dissociation Kit (Miltenyi Biotec). After blocking with FcBlock, cells were stained with antibodies against CD45, CD3, and CD8 to identify cytotoxic T cells, or CD11c and CD86 to evaluate the maturation of dendritic cells. Data acquisition and analysis were performed using FlowJo software.

Systemic safety was evaluated through comprehensive hematological and biochemical analysis of blood samples collected at the end of the treatment period. Blood was centrifuged at 3000 rpm for 20 min to separate serum for measuring liver enzymes (ALT, AST, ALP) and the kidney function marker (BUN). Additionally, complete blood counts including WBC, PLT, Neu%, and Lym% were quantified using a hematology analyzer to ensure all parameters remained within normal physiological ranges.

### 4.8. Animal ethics statement

All animal experiments were carried out in compliance with the relevant regulations of the Institutional Animal Care and Use Committee (IACUC) at Ewha Womans University (approval no. EWHA IACUC 22–073-2).

### 4.9. Statistical analysis

Statistical significance between two groups was assessed using Student's *t*-test. For comparisons involving more than two groups, one-way analysis of variance (ANOVA) was applied, followed by Tukey-Kramer post-hoc tests for multiple comparisons. Survival data were analyzed using Kaplan-Meier curves and the log-rank test. All results are presented as mean ± standard deviation (SD), with *p*-values indicated as follows: ns = no significance, $*p < 0.05$, $**p < 0.01$, $***p < 0.001$, $****p < 0.0001$. The sample size (n) for each analysis and the detailed statistical methods are provided in the figure legends.

## CRediT authorship contribution statement

**Hwanju Lim:** Visualization, Methodology, Investigation, Formal analysis. **Yujeong Moon:** Writing – original draft, Validation, Formal analysis, Data curation. **Sangheon Han:** Visualization, Formal analysis, Data curation. **Hanhee Cho:** Writing – original draft, Visualization, Data curation, Conceptualization. **Sunejeong Song:** Investigation. **Jinseong Kim:** Formal analysis. **Jagyeong Goo:** Validation. **Nayeon Shim:** Validation. **Lili Guo:** Methodology. **Tae-il Kim:** Validation. **Won Seok Chang:** Validation, Supervision, Resources. **Won-Gun Koh:** Supervision, Resources, Data curation. **Kwangmeyung Kim:** Writing – review & editing, Supervision, Resources, Project administration, Funding acquisition, Conceptualization.

## Declaration of competing interest

The authors declare no conflict of interest.

## Acknowledgements

This work was supported by the National Research Foundation of Korea (NRF) grant funded by the Korea government (MSIT) (RS-2022-NR068161, RS-2025-02219039).

## Appendix A. Supplementary data

Supplementary data to this article can be found online at https://doi.org/10.1016/j.jconrel.2026.114750.

## Data availability

All data obtained throughout this study are presented in the manuscript or supporting information.

## References

[1] A.R.T. Bergin, S. Loi, Triple-negative breast cancer: recent treatment advances, F1000Res 8 (2019).
[2] F. Derakhshan, J.S. Reis-Filho, Pathogenesis of triple-negative breast cancer, Annu. Rev. Pathol. 17 (2022) 181–204.
[3] F. Dong, et al., M2 macrophage-induced lncRNA PCAT6 facilitates tumorigenesis and angiogenesis of triple-negative breast cancer through modulation of VEGFR2, Cell Death Dis. 11 (9) (2020).
[4] K.A. Won, C. Spruck, Triple-negative breast cancer therapy: current and future perspectives (review), Int. J. Oncol. 57 (6) (2020) 1245–1261.
[5] A.C. Wolff, et al., Recommendations for human epidermal growth factor receptor 2 testing in breast cancer: American Society of Clinical Oncology/College of American Pathologists clinical practice guideline update, J. Clin. Oncol. 31 (31) (2013) 3997–4013.

[6] C. Liedtke, et al., Response to neoadjuvant therapy and long-term survival in patients with triple-negative breast cancer, J. Clin. Oncol. 26 (8) (2008) 1275–1281.
[7] P. Karmacharya, et al., Fabrication of poly-L-histidine-coated mesoporous silica nanoparticles with hyaluronic acid for targeted doxorubicin delivery, J. Pharm. Investig. (2025), https://doi.org/10.1007/s40005-025-00773-3.
[8] S. Lim, et al., Recent advances and challenges of repurposing nanoparticle-based drug delivery systems to enhance cancer immunotherapy, Theranostics 9 (25) (2019) 7906–7923.
[9] G. Ma, S.B. Yang, J. Park, Recent development and challenges in carrier-free nanomedicines, J. Pharm. Investig. 56 (2025) 151–.170.
[10] T. Okusaka, et al., Phase II study of radiotherapy combined with gemcitabine for locally advanced pancreatic cancer, Br. J. Cancer 91 (4) (2004) 673–677.
[11] M. Tempero, et al., Randomized phase II comparison of dose-intense gemcitabine: thirty-minute infusion and fixed dose rate infusion in patients with pancreatic adenocarcinoma, J. Clin. Oncol. 21 (18) (2003) 3402–3408.
[12] Y.C. Kil, et al., Immune-chemo combination therapy using doxorubicin/viral epitope Pluronic nanoparticles, J. Pharm. Investig. (2025), https://doi.org/10.1007/s40005-025-00781-3.
[13] J. Ohana, et al., Transformation of immunosuppressive mtKRAS tumors into immunostimulatory tumors by Nerofe and doxorubicin, Oncotarget 14 (1) (2023).
[14] R. Barnestein, et al., Immunosuppressive tumor microenvironment modulation by chemotherapies and targeted therapies to enhance immunotherapy effectiveness, Oncoimmunology 11 (1) (2022) 2120676.
[15] A. Bandyopadhyay, et al., Doxorubicin in combination with a small TGFbeta inhibitor: a potential novel therapy for metastatic breast cancer in mouse models, PLoS One 5 (4) (2010) e10365.
[16] T.M. Allen, P.R. Cullis, Liposomal drug delivery systems: from concept to clinical applications, Adv. Drug Deliv. Rev. 65 (1) (2013) 36–48.
[17] N. Shim, et al., Recent developments in chemodrug-loaded nanomedicines and their application in combination cancer immunotherapy, J. Pharm. Investig. 54 (1) (2024) 13–36.
[18] K.N. Syrigos, et al., A phase-II study of liposomal doxorubicin and docetaxel in patients with advanced pancreatic cancer, Anticancer Res. 22 (6B) (2002) 3583–3588.
[19] C. Mamot, et al., Liposome-based approaches to overcome anticancer drug resistance, Drug Resist. Updat. 6 (5) (2003) 271–279.
[20] V. Makwana, et al., Liposomal doxorubicin as targeted delivery platform: current trends in surface functionalization, Int. J. Pharm. 593 (2021).
[21] S. Wilhelm, et al., Analysis of nanoparticle delivery to tumours, Nat. Rev. Mater. 1 (5) (2016).
[22] J. Kim, et al., Perspectives for improving the tumor targeting of nanomedicine via the EPR effect in clinical tumors, Int. J. Mol. Sci. 24 (12) (2023).
[23] V.P. Torchilin, Multifunctional nanocarriers, Adv. Drug Deliv. Rev. 58 (14) (2006) 1532–1555.
[24] E.I. Azzam, J.-P. Jay-Gerin, D. Pain, Ionizing radiation-induced metabolic oxidative stress and prolonged cell injury, Cancer Lett. 327 (1) (2012) 48–60.
[25] J.T. McDonald, et al., Ionizing radiation activates the Nrf2 antioxidant response, Cancer Res. 70 (21) (2010) 8886–8895.
[26] I.I. Verginadis, et al., Radiotherapy toxicities: mechanisms, management, and future directions, Lancet 405 (10475) (2025) 338–352.
[27] M.S. Moran, Radiation therapy in the locoregional treatment of triple-negative breast cancer, Lancet Oncol. 16 (3) (2015) e113–e122.
[28] H. Song, et al., Gadolinium-based ultra-small nanoparticles augment radiotherapy-induced T-cell response to synergize with checkpoint blockade immunotherapy, Nanoscale 14 (31) (2022) 11429–11442.
[29] N.A. Thornberry, et al., A combinatorial approach defines specificities of members of the caspase family and granzyme B. Functional relationships established for key mediators of apoptosis, J. Biol. Chem. 272 (29) (1997) 17907–17911.
[30] S.W. Chung, et al., Albumin-binding caspase-cleavable prodrug that is selectively activated in radiation exposed local tumor, Biomaterials 94 (2016) 1–8.
[31] H.R. Kim, et al., Stimulating macropinocytosis of peptide-drug conjugates through DNA-dependent protein kinase inhibition for treating KRAS-mutant cancer, J. Control. Release 372 (2024) 176–193.
[32] H.R. Kim, et al., Synergistic anticancer immunity in metastatic triple-negative breast cancer through an in situ amplifying peptide-drug conjugate, J. Control. Release 375 (2024) 681–697.
[33] Y.S. Cho, et al., Sustained potentiation of bystander killing via PTEN-loss driven macropinocytosis targeted peptide-drug conjugate therapy in metastatic triple-negative breast cancer, Biomaterials 289 (2022) 121783.
[34] H.R. Kim, et al., Caspase-3 mediated switch therapy of self-triggered and long-acting prodrugs for metastatic TNBC, J. Control. Release 346 (2022) 136–147.
[35] Y.S. Cho, et al., Macropinocytosis-targeted peptide-docetaxel conjugate for bystander pancreatic cancer treatment, J. Control. Release 376 (2024) 829–841.
[36] J. Kim, et al., Micro-syringe chip-guided intratumoral administration of lipid nanoparticles for targeted anticancer therapy, Biomater. Res. 27 (1) (2023) 102.
[37] S. Nahar, et al., Regression and eradication of triple-negative breast carcinoma in 4T1 mouse model by combination immunotherapies, Cancers (Basel) 15 (8) (2023).
[38] G. Xie, et al., Local angiotensin II contributes to tumor resistance to checkpoint immunotherapy, J. Immunother. Cancer 6 (1) (2018) 88.
[39] W. Um, et al., Visible light-induced apoptosis activatable nanoparticles of photosensitizer-DEVD-anticancer drug conjugate for targeted cancer therapy, Biomaterials 224 (2019) 119494.
[40] B.S. Lee, et al., Induced phenotype targeted therapy: radiation-induced apoptosis-targeted chemotherapy, JNCI J. Natl. Cancer Inst. 107 (2) (2015) dju403.
[41] L. Zhang, et al., Pharmacokinetics, distribution and anti-tumor efficacy of liposomal mitoxantrone modified with a luteinizing hormone-releasing hormone receptor-specific peptide, Int. J. Nanomedicine 13 (2018) 1097–1105.
[42] A. Gabizon, D. Papahadjopoulos, Liposome formulations with prolonged circulation time in blood and enhanced uptake by tumors, Proc. Natl. Acad. Sci. USA 85 (18) (1988) 6949–6953.
[43] X. Wu, et al., Enhanced in vivo stability and antitumor efficacy of PEGylated liposomes of paclitaxel palmitate prodrug, Int. J. Nanomedicine 19 (2024) 11539–11560.
[44] J.H. Lee, Y.M. Lee, J.W. Park, Regulation of ionizing radiation-induced apoptosis by a manganese porphyrin complex, Biochem. Biophys. Res. Commun. 334 (2) (2005) 298–305.
[45] J.K. Leach, et al., Ionizing radiation-induced, mitochondria-dependent generation of reactive oxygen/nitrogen, Cancer Res. 61 (10) (2001) 3894–3901.
[46] X. An, et al., Oxidative cell death in cancer: mechanisms and therapeutic opportunities, Cell Death Dis. 15 (8) (2024) 556.
[47] Z. Zheng, et al., Mechanisms and applications of radiation-induced oxidative stress in regulating cancer immunotherapy, Front. Immunol. 14 (2023) 1247268.
[48] K. Boland, L. Flanagan, J.H. Prehn, Paracrine control of tissue regeneration and cell proliferation by Caspase-3, Cell Death Dis. 4 (7) (2013) e725.
[49] M. D'Amelio, V. Cavallucci, F. Cecconi, Neuronal caspase-3 signaling: not only cell death, Cell Death Differ. 17 (7) (2010) 1104–1114.
[50] I. Dingjan, et al., Lipid peroxidation causes endosomal antigen release for cross-presentation, Sci. Rep. 6 (2016) 22064.
[51] T. Nakazawa, S. Nagatsuka, Radiation-induced lipid peroxidation and membrane permeability in liposomes, Int. J. Radiat. Biol. Relat. Stud. Phys. Chem. Med. 38 (5) (1980) 537–544.
[52] W. Jung, et al., Design and material for a patternable polysiloxane acrylate-based penetrating intracortical neural probe, J. Micromech. Microeng. 31 (3) (2021).
[53] S.K. Bhagavatula, et al., An interventional image-guided microdevice implantation and retrieval method for in-vivo drug response assessment, Med. Phys. 46 (11) (2019) 5134–5143.
[54] H.K. Koblish, et al., Characterization of INCB086550: a potent and novel small-molecule PD-L1 inhibitor, Cancer Discov. 12 (6) (2022) 1482–1499.
[55] M.K. Shim, et al., Cancer-specific drug-drug nanoparticles of pro-apoptotic and cathepsin B-cleavable peptide-conjugated doxorubicin for drug-resistant cancer therapy, Biomaterials 261 (2020) 120347.